

# Application of the FUN3D Solver to the 4th AIAA Drag Prediction Workshop

E. M. Lee-Rausch,\* D. P. Hammond,† E. J. Nielsen,‡ S. Z. Pirzadeh,§ and C. L. Rumsey¶  
*NASA Langley Research Center, Hampton, Virginia 23681*

DOI: 10.2514/1.C032558

FUN3D Navier–Stokes solutions were computed for the 4th AIAA Drag Prediction Workshop grid-convergence study, downwash study, and Reynolds-number study on a set of node-based mixed-element grids. All of the baseline tetrahedral grids were generated with the VGRID (developmental) advancing-layer and advancing-front grid-generation software package following the gridding guidelines developed for the workshop. With maximum grid sizes exceeding 100 million nodes, the grid-convergence study was particularly challenging for the node-based unstructured grid generators and flow solvers. At the time of the workshop, the super-fine grid with 105 million nodes and 600 million tetrahedral elements was the largest grid known to have been generated using VGRID. FUN3D Version 11.0 has a completely new pre- and postprocessing paradigm that has been incorporated directly into the solver and functions entirely in a parallel, distributed-memory environment. This feature allowed for practical preprocessing and solution times on the largest unstructured-grid size requested for the workshop. For the constant-lift grid-convergence case, the convergence of total drag is approximately second-order on the finest three grids. The variation in total drag between the finest two grids is only two counts. At the finest grid levels, only small variations in wing and tail pressure distributions are seen with grid refinement. Similarly, a small wing side-of-body separation also shows little variation at the finest grid levels. Overall, the FUN3D results compare well with the structured-grid code CFL3D. For the grid-convergence case, the FUN3D total and component forces/moments are within one standard deviation of the workshop core solution medians and are very close to the median values especially at the finest grid levels. The FUN3D downwash study and Reynolds-number study results also compare well with the range of results shown in the workshop presentations.

## I. Introduction

THE Fourth International AIAA Drag Prediction Workshop (DPW-IV) was held in San Antonio, Texas, in June 2009 to evaluate computational fluid dynamics (CFD) transonic cruise drag predictions for subsonic transport aircraft [1]. The objectives of the workshop were as follows: 1) to build on the success of past AIAA Drag Prediction Workshops [2–4], 2) to assess the state-of-the-art computational methods as practical aerodynamic tools for aircraft force and moment prediction of industry-relevant geometries, 3) to provide an impartial forum for evaluating the effectiveness of existing computer codes and modeling techniques using Navier–Stokes solvers, and 4) to identify areas needing additional research and development. The focus of this particular workshop was on “blind” drag prediction (a priori experimental data were not available for comparison) for the NASA Common Research Model (CRM) transonic wing–body–tail configuration [5]. As with prior Drag Prediction Workshops, grid convergence of the force and moments coefficients was evaluated at the design cruise Mach number and lift coefficient. With maximum grid sizes exceeding 100 million nodes (600 million tetrahedral cells), the grid-convergence study was particularly challenging for the node-based unstructured grid generators and flow solvers. This maximum grid size was four times larger than required for DPW-III. Additionally, in this workshop, the drag increment due to the trimming of the aircraft and drag increment

due to Reynolds-number scaling were evaluated. An optional Mach sweep study was also requested to look at drag rise.

An experimental aerodynamic investigation of the NASA CRM has been conducted in the NASA Langley National Transonic Facility [6] and in the NASA Ames 11 ft Transonic Wind Tunnel [7]. A large offset in pitching moment between the experimental data and the computational data from DPW-IV was noted. Subsequent computational assessments of the model support system interference effects indicated that the CRM pitching moment is sensitive to the presence of the mounting hardware [8,9]. The investigations of [9] also lead to the discovery of a large discrepancy in the as-built wind-tunnel model wing twist. Because of the differences between the wind-tunnel geometry and the DPW-IV geometry, one-to-one comparisons between the DPW-IV cases and the experimental data are problematic. However, as with previous DPW workshops, the DPW-IV test cases have become standard CFD test cases. Eliasson and Peng have published a paper looking at the influence of turbulence modeling and grid resolution in computations of the CRM [10]. Hashimoto et al. have used the CRM to evaluate a hexahedra grid-generation method [11].

Results from the DPW-IV grid-convergence study, downwash study, and Reynolds-number study were submitted to the workshop for the FUN3D [12–14] unstructured-grid Navier–Stokes flow solver on a set of node-based mixed-element grids. This paper gives a summary of the FUN3D results submitted to the workshop. A description of the unstructured node-based grids is provided in this paper detailing the grid parameters and spacings. Some improvements to the FUN3D solver/grid processing efficiency and parallelization are also discussed. These improvements allowed for the practical processing of the largest unstructured grid sizes requested for the workshop (100 million nodes). Because of the differences between the wind-tunnel geometry and the DPW-IV geometry, comparisons are made with overset structured grid results from the well known code CFL3D [15] and with results from the statistical analysis of the workshop [16].

## II. Fourth International AIAA Drag Prediction Workshop Cases

All of the DPW-IV workshop cases are based on the analysis of the NASA CRM wing–body–tail configuration shown in Fig. 1. The

Presented as Paper 2010-4551 at the 28th AIAA Applied Aerodynamics Conference, Chicago, IL, 28 June–1 July 2010; received 5 August 2013; accepted for publication 30 October 2013; published online 14 February 2014. This material is declared a work of the U.S. Government and is not subject to copyright protection in the United States. Copies of this paper may be made for personal or internal use, on condition that the copier pay the \$10.00 per-copy fee to the Copyright Clearance Center, Inc., 222 Rosewood Drive, Danvers, MA 01923; include the code 1542-3868/14 and \$10.00 in correspondence with the CCC.

\*Research Engineer. Senior Member AIAA.

†Senior Research Scientist.

‡Senior Research Scientist. Senior Member AIAA.

§Senior Research Engineer. Senior Member AIAA (Posthumous).

¶Senior Research Scientist. Associate Fellow AIAA.

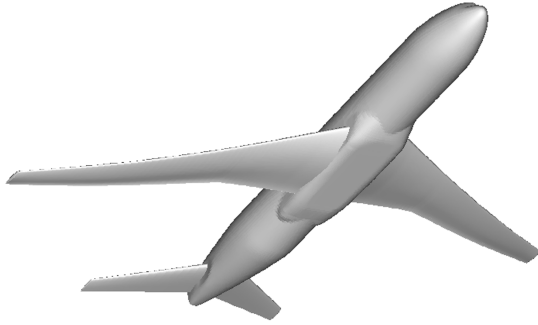


Fig. 1 NASA CRM wing-body-tail configuration.

configuration is a transonic transport aircraft designed to fly at a cruise Mach number of  $M_\infty = 0.85$  with a nominal lift condition of  $C_L = 0.500$  at a Reynolds number of  $Re_c = 40 \times 10^6$  per mean aerodynamic chord  $c_{ref}$ . The reference geometric quantities for the CRM are summarized in Table 1. A detailed description of the CRM can be found in [5]. The first test case (case 1) for the workshop included a grid-convergence study and a downwash study. For the grid-convergence study, computations were performed for a constant design-lift coefficient of  $C_L = 0.500 \pm 0.001$  at a freestream Mach number of  $M_\infty = 0.85$  and freestream chord Reynolds number of  $Re_c = 5 \times 10^6$ . (Note that this Reynolds number represented a planned wind-tunnel test condition.) For the grid-convergence study, a nominal tail incidence angle  $i_h = 0$  deg was specified. A family of four grids was required for the study, with consistent levels of refinement between each grid: coarse (3.5 million nodes), medium (10 million nodes), fine (35 million nodes), and super-fine (100 million nodes). The downwash study required complete angle-of-attack sweeps for the CRM with three different tail settings ( $i_h = -2, 0, +2$  deg) on a set of medium-sized grids. The trimmed drag polar was then derived from an interpolation of the polars at the variable tail incidences using a process provided by the organizing committee. The delta drag polar was then computed by differencing the polar results from a tail-off configuration with results from the trimmed tail-on drag polar. The optional Reynolds-number study (case 3) is a comparison of  $Re_c = 5 \times 10^6$  results with  $Re_c = 20 \times 10^6$  results on the medium grid size at the design Mach number and lift condition ( $M_\infty = 0.85$  and  $C_L = 0.500 \pm 0.001$ ). For case 3, the nominal tail incidence angle  $i_h = 0$  deg was used. FUN3D results were not computed for the optional Mach sweep study (case 2).

### III. Workshop Unstructured Langley Research Center Node-Based Grids

The FUN3D solutions were computed using a mixed-element version of the vertex-based unstructured tetrahedral grids generated for the workshop. The tetrahedral grids are available on the DPW-IV website under the label “unstructured LaRC/NodeBase” [1]. All of the baseline tetrahedral grids were generated with the VGRID (developmental) advancing-layer and advancing-front grid-generation software package [17] following the gridding guidelines developed for the workshop [1]. The grids generated with VGRID were fully tetrahedral. However, VGRID uses an advancing layer technique to generate the boundary-layer portion of the grid so that prisms can be reconstructed in the boundary layer for use with a mixed-element discretization. In the boundary layer, three tetrahedral

cells are combined into one prism. The mixed-element grids have essentially the same number of nodes and nodal spacing as the fully tetrahedral grids, although the number of cells and the shape of the control volumes differ in the boundary layers. The merging process adds a trivial number of node points in the interface region between the advancing layers and advancing front to construct a valid topology in the interface region between the prismatic layers and the tetrahedral region. For the LaRC node-based grids, the merging process also reduces the total number of cells in the grid by a factor of approximately 1/2 to 2/3.

For the grid-convergence study, a set of four globally refined grids were generated following the gridding guidelines. Similarly, for the downwash study, a set of three consistently sized grids with varying tail incidences were generated. For the tail-off configuration, the tail solid surfaces were removed, and the volume grid was regenerated with the same spacing requirements in the location of the tail as were used in the tail-on configuration. A summary of the case 1 mixed-element grid sizes and runs is shown in Table 2. For the case 3 high-Reynolds-number grid, the surface grid distribution from the case 1 medium grid was used with a smaller minimum wall spacing. The total number of grid nodes for the  $Re_c = 20 \times 10^6$  grid was 11 million. Note that, at the time of the workshop, the case 1 super-fine grid with 105 million nodes and 600 million tetrahedral elements was the largest grid known to have been generated using VGRID. (Note that the mixed-element version of the super-fine grid contained 401 million cells.)

VGRID has two types of spacing requirements; the “inviscid” spacing distributions are used in the advancing-front region of the mesh, and the “viscous” spacing distributions are used in the advancing-layer regions of the mesh where high stretching is required. The different grids for the grid refinement study were generated by a global coarsening/refinement of the inviscid spacing parameters (VGRID “sources”) and a global coarsening/refinement of the viscous wall spacing. A summary of characteristic grid spacing for the wing-body-tail ( $i_h = 0$  deg) configuration is shown in Table 3 to illustrate that the grids were generated following the gridding guidelines for the workshop. The global spacing factor shown in Table 3 represents the relative coarsening/refinement of the inviscid spacing parameters for each of the grids. The range of chordwise spacing for the wing and tail leading edge (LE) and trailing edge (TE) fall close to the 0.1% local chord specified for the medium grids at the root chord  $c_{root}$  and tip chord  $c_{tip}$  locations. The spanwise stretching of the grids was 10:1 near the wing LE and 15:1 near the wing TE. There were similar limits on the spanwise stretching near the tail LE and TE. The limits on the grid spanwise stretching rates keep the wing and tail spanwise spacing at the root and tip well within the workshop requirement (0.1% local semispan for the medium grid). A composite view of the medium-grid wing-body-tail grid is shown in Fig. 2 to illustrate the overall topology of the surface mesh.

The clustering of points normal to the surface was computed according to the VGRID stretching function [18]

Table 2 Summary of DPW-IV case 1 mesh sizes and runs at  $M_\infty = 0.85$ ,  $Re_c = 5 \times 10^6$

Grid	Tail incidence, deg	Grid size (millions of nodes)	$C_L = 0.500$	Alpha polar
Coarse	0	3.7	Required	Not required
Medium	0	10.3	Required	Required
Fine	0	35.5	Required	Not required
Super fine	0	105.7	Required	Not required
Medium	-2	10.3	Not required	Required
Medium	+2	10.3	Not required	Required
Medium	No tail	8.2	Not required	Required

Table 1 Reference geometry for the CRM

Parameter	Value
Mean aerodynamic chord	275.80 in.
Wing reference area/2	297,360 in. <sup>2</sup>
Wing span/2	1159.0 in.
Aspect ratio	9.0

**Table 3** Summary of characteristic grid spacing for the wing-body-tail  $i_h = 0$  deg grids

	Node-centered grids			
	Coarse	Medium	Fine	Super fine
Global spacing factor	1.654	1.00	0.562	0.355
Percent chordwise	$0.20\%c_{\text{root}}$	$0.12\%c_{\text{root}}$	$0.07\%c_{\text{root}}$	$0.04\%c_{\text{root}}$
Spacing at wing LE	$0.20\%c_{\text{tip}}$	$0.12\%c_{\text{tip}}$	$0.07\%c_{\text{tip}}$	$0.04\%c_{\text{tip}}$
Percent chordwise	$0.07\%c_{\text{root}}$	$0.04\%c_{\text{root}}$	$0.02\%c_{\text{root}}$	$0.01\%c_{\text{root}}$
Spacing at wing TE	$0.12\%c_{\text{tip}}$	$0.07\%c_{\text{tip}}$	$0.04\%c_{\text{tip}}$	$0.02\%c_{\text{tip}}$
Percent chordwise	$0.20\%c_{\text{root}}$	$0.16\%c_{\text{root}}$	$0.09\%c_{\text{root}}$	$0.06\%c_{\text{root}}$
Spacing at tail LE	$0.26\%c_{\text{tip}}$	$0.12\%c_{\text{tip}}$	$0.07\%c_{\text{tip}}$	$0.04\%c_{\text{tip}}$
Percent chordwise	$0.20\%c_{\text{root}}$	$0.12\%c_{\text{root}}$	$0.07\%c_{\text{root}}$	$0.04\%c_{\text{root}}$
Spacing at tail TE	$0.20\%c_{\text{tip}}$	$0.12\%c_{\text{tip}}$	$0.07\%c_{\text{tip}}$	$0.04\%c_{\text{tip}}$
Wing/tail TE cells	8/8	12/12	16/16	24/24
Spacing fuselage nose/aft body	$4.0\%c_{\text{ref}}$	$2.4\%c_{\text{ref}}$	$1.3\%c_{\text{ref}}$	$0.9\%c_{\text{ref}}$
Average cell $y^+$	1.0	0.667	0.444	0.296
Nominal prism layer cells	25	25	25	25
Viscous wall spacing $\delta_1$ , in.	0.001478	0.0009850	0.0006570	0.0004380
Viscous stretching $r_1$ , $r_2$	0.12, 0.02	0.12, 0.02	0.12, 0.02	0.12, 0.02
Outer boundary box	$100c_{\text{ref}}$	$100c_{\text{ref}}$	$100c_{\text{ref}}$	$100c_{\text{ref}}$

$$\delta_n = \delta_1 [1 + r_1 (1 + r_2)^{n-1}]^{n-1} \quad (1)$$

where  $\delta_n$  is the normal spacing of the  $n$ th layer,  $\delta_1$  is the spacing of the first layer, and the factors  $r_1$  and  $r_2$  are constants that determine the rate of stretching. (Note that, if  $r_2$  is zero, then the stretching is geometric.) Based on the advancing layer stretching factors given in Table 3, the maximum growth rate of the cell sizes in the viscous layers is approximately 1.19, which is less than the 1.25 requested in the gridding guidelines. The blunt trailing edges of the wing and nacelles were resolved in all grids by explicitly dividing the trailing-edge surfaces into the specified number of cells.

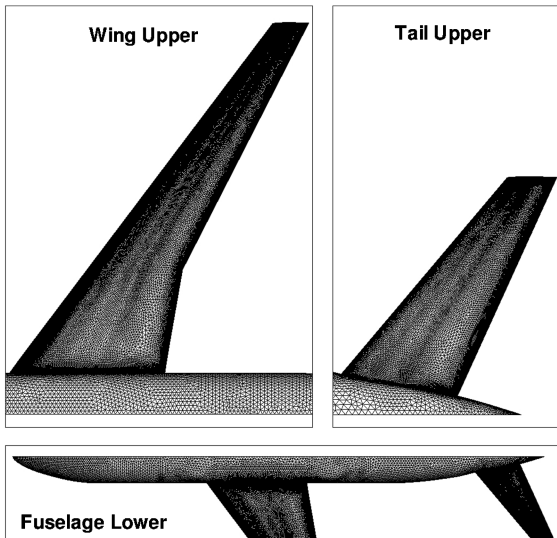
#### IV. FUN3D Flow Solver

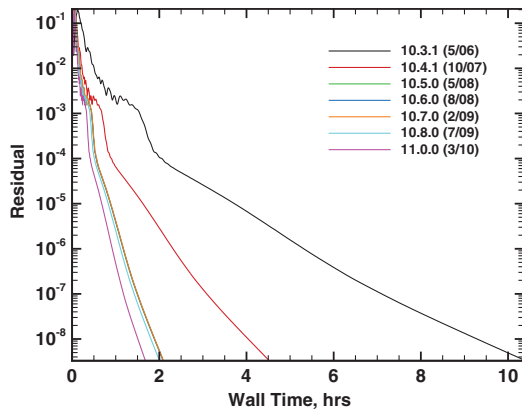
FUN3D [12–14] is a finite-volume Reynolds-averaged Navier–Stokes (RANS) solver in which the flow variables are stored at the vertices or nodes of the mesh. FUN3D solves the equations on mixed-element grids, including tetrahedra, pyramids, prisms, and hexahedra, and it has a two-dimensional path for triangular/quadrilateral grids. It employs an implicit upwind algorithm in which

the inviscid fluxes are obtained with a flux-difference-splitting scheme. At interfaces delimiting neighboring control volumes, the inviscid fluxes are computed using an approximate Riemann solver based on the values on either side of the interface. Several convective flux schemes are available in FUN3D. The most common scheme for subsonic and transonic flows is Roe's flux-difference splitting [19], which is used in the current study. For second-order accuracy, interface values are obtained by extrapolation of the control volume centroidal values, based on gradients computed at the mesh vertices using an unweighted least-squares technique. Several flux limiters are available in FUN3D to limit the reconstructed values when necessary. The most common used for transonic flows is that of Venkatakrishnan [20], which is used in this study. For tetrahedral meshes, the full viscous fluxes are discretized using a finite-volume formulation in which the required velocity gradients on the dual faces are computed using the Green–Gauss theorem. On tetrahedral meshes, this is equivalent to a Galerkin-type approximation. For nontetrahedral meshes, the same Green–Gauss approach can lead to odd–even decoupling. A pure edge-based approach can be used to circumvent the odd–even decoupling issue but yields only approximate viscous terms. Thus, for nontetrahedral meshes, the edge-based gradients are combined with Green–Gauss gradients, which improves the h-ellipticity of the operator and allows the complete viscous stresses to be evaluated [21,22]. This formulation results in a consistent discretization of the full Navier–Stokes equations.

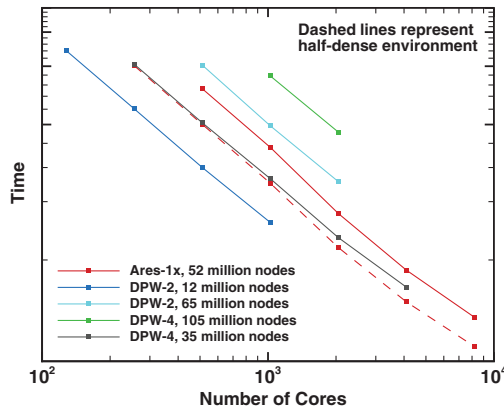
The solution at each time step is updated with a backward Euler time-differencing scheme. At each time step, the linear system of equations is approximately solved with either a multicolor point-implicit procedure or an implicit-line relaxation scheme [23]. Local time-step scaling is employed to accelerate convergence to steady state. For turbulent flows, several models are available within FUN3D. The most common are the one-equation model of Spalart–Allmaras (SA) [24] and the two-equation shear stress transport (SST) model of Menter [25]. The SA model may be solved loosely coupled to the mean-flow equations or tightly coupled to the mean-flow equations. The Menter SST model [25] is loosely coupled. The multicolor point-implicit solution procedure and loosely coupled SA model are used for the current study.

Efforts were initiated in the summer of 2006 to improve the computational performance of the FUN3D code. Many low-level aspects of the code were examined, including cache reuse, message-passing interface (MPI) communication, inlining, basic blocks, and alternative ordering techniques for the grid/linear algebra operations. The result of this effort was a factor of 6.5 speed-up of Version 11.0 over Version 10.3.1 (May 2006). The code performance at several points in time from May 2006 to Version 11.0 is shown in Fig. 3a. The comparison of density residual versus wall clock time shows a 6.5 times speed-up for a wing-body transonic Navier–Stokes solution to the same level of residual convergence. This timing study was performed with fixed compiler, compiler options, computer hardware, and solver options so that all of the code speed-up shown is due to computer science and implementation differences. The FUN3D multicolor point-implicit solver has demonstrated linear scaling in parallel efficiency up to 8192 computer cores on the Pleiades supercomputer at the NASA Advanced Supercomputing (NAS) facility. Pleiades is a Silicon Graphics, Inc. (SGI) distributed-memory Integrated Computer Environment system with Xeon E5472 and X5570 processor cores. This scaling study used the Xeon E5272 processors with two quad-core processors per node and 8 GB of memory per node. Figure 3b shows the parallel scalability of the Version 11.0 code on a range of grid sizes including the DPW-IV 105-million-mesh super-fine mesh described in the previous section. Grids from the second DPW (DPW-II) and the Ares-1X launch vehicle are also included in Fig. 3b. Most of the results shown were run fully dense, namely, one process per core (e.g., eight processes on a dual-quad node). One timing study for the Ares-1X was run in a half-dense environment (four processes on a dual-quad node) to illustrate the speed-up from decreasing the interprocessor communication. The solutions for the timing study were not run to convergence, and so no absolute times are provided in Fig. 3b. The

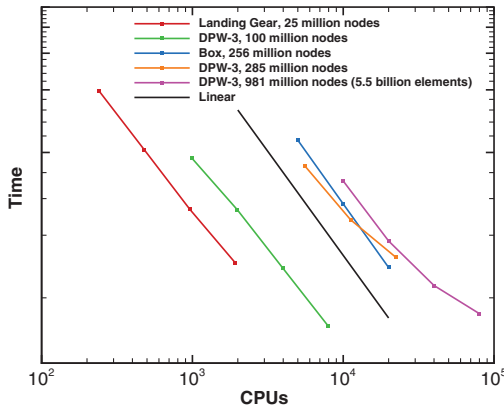
**Fig. 2** Surface grid for the CRM wing-body-tail medium-sized grid (10.3 million nodes).



a) Computational timing



b) Parallel scalability for v11.0



c) Parallel scalability for v12.3

Fig. 3 FUN3D computational performance.

FUN3D solver has also demonstrated good scaling in parallel efficiency up to 80,000 computer cores on the Titan Cray XK7 system at the U.S. Department of Energy's Oak Ridge National Laboratory. Titan is a hybrid supercomputer with a combination of 299,008 AMD Opteron 6274 CPU cores and 18,688 NVIDIA Tesla graphic processing units. This scaling study used the 7274 Opteron processors with 16 processors per node and 32 GB of memory per node. Figure 3c shows the parallel scalability of the Version 12.3 code on a range of grid sizes, including a DPW-III grid with 981 million nodes and 5.5 billion elements. Similarly, the solutions for the timing study were not run to convergence, and so no absolute times are provided in Fig. 3c.

As of Version 11.0, FUN3D also has a completely new pre- and postprocessing paradigm that has been incorporated directly into the solver and functions entirely in a parallel, distributed-memory environment. The result is an end-to-end scalable approach that eliminates hardware constraints as problem sizes grow. The new

paradigm also cuts down on pre- and postprocessing times considerably and greatly simplifies the use of FUN3D. For the 105-million-node tetrahedral grid, grid partitioning and preprocessing took approximately 8 min using 1024 cores on Pleiades. Partitioning the same grid on 1024 processors using a serial preprocessor previously required two weeks using 800 GB of shared memory on the NAS Columbia supercomputer, which has SGI Altix 3700/4700 cores with approximately 2 GB of memory per core. A substantial decrease in I/O processing time, and I/O memory overhead, was seen using either of the two new I/O options within Version 11.0 (i.e., FORTRAN stream I/O, MPI/IO).

## V. Computational Results

The FUN3D workshop results were computed using the full Navier–Stokes equations with the flux-difference-splitting scheme of Roe, the Venkatakrishnan flux limiter, and the loosely coupled SA turbulence model on mixed-element grids (prisms through the boundary layer, tetrahedra in the far field). In accordance with the workshop specifications, all computations assume fully turbulent flow. For all cases, local time-step scaling was used to accelerate the residual convergence of the nonlinear equations and achieve steady-state values of forces and moments. For the constant-lift cases, the angle of attack (AOA) was relaxed based on the difference in total lift and the target lift during the convergence history. The AOA is updated at every iteration, which can slow the solution convergence as compared to a case where the AOA is constant. Good solution residual, force, and moment convergence was achieved for all the workshop computations even on the super-fine grid size. Figure 4 shows the nonlinear solution residual, force, and moment convergence histories for the medium and super-fine grids. The L2 norm of the density ( $R_1$ ) residual and the turbulence model ( $R_6$ ) residual are shown for each local time step.

Total force and moment results for the CRM grid-convergence study are given in Fig. 5. The angle of attack, total drag  $C_D$ , pressure drag  $C_{Dp}$ , skin friction drag  $C_{Dsf}$  and pitching moment  $C_{My}$  are plotted versus  $N^{-2/3}$ , where  $N$  is the number of nodes for the unstructured grid. (In the asymptotic range, one would expect a linear variation in forces or moments with  $N^{-2/3}$  for a second-order scheme for a family of three-dimensional grids that are globally refined.) Thus, results using finer grids appear to the left in the figures, and results using coarser grids appear to the right. The variation in total drag on the finest three grids is about six counts, and the variation on the finest two grids is two counts. The decomposition of the drag into pressure and skin friction components illustrates that the majority of the variation is due to the pressure component. Although the changes in drag and AOA are nearly linear on the finest three grids, the change in pitching moment is not, possibly due to the sensitivity of the wing pitching moment to shock strength.

The FUN3D results from the grid-convergence study are compared in Fig. 5 to results from a well known structured-grid code, CFL3D [26], and with results from the statistical analysis of the workshop [16]. The CFL3D results were computed on a set of overset grids using an upwind algorithm, the SA turbulence model, and the thin-layer approximation of the RANS equations. A complete description of the overset grids and CFL3D results can be found in [15]. (Note that the CFL3D results from [15] were not submitted to the workshop.) The median values and estimates of standard deviations for the case 1 core solutions at three grid levels [16] are also compared with the FUN3D results in Fig. 5. The median values plus and minus one standard deviation are shown in the plots. The statistical analysis of workshop submissions in [16] identified outliers that were different from the other solutions. The outliers are identified as those solutions (AOA, total drag, and total pitching moment) outside the upper and lower scatter limits (the median values plus and minus the standard deviation multiplied by a coverage factor of  $\sqrt{3}$ ). The core solutions are the complete solution sets minus the outliers. For DPW-IV, there are 21 solutions in the core set. The FUN3D results in Fig. 5 are within one standard deviation of the core solution medians and are very close to the median values, especially at the finest grid levels. Overall, the comparison between the computed forces and moments

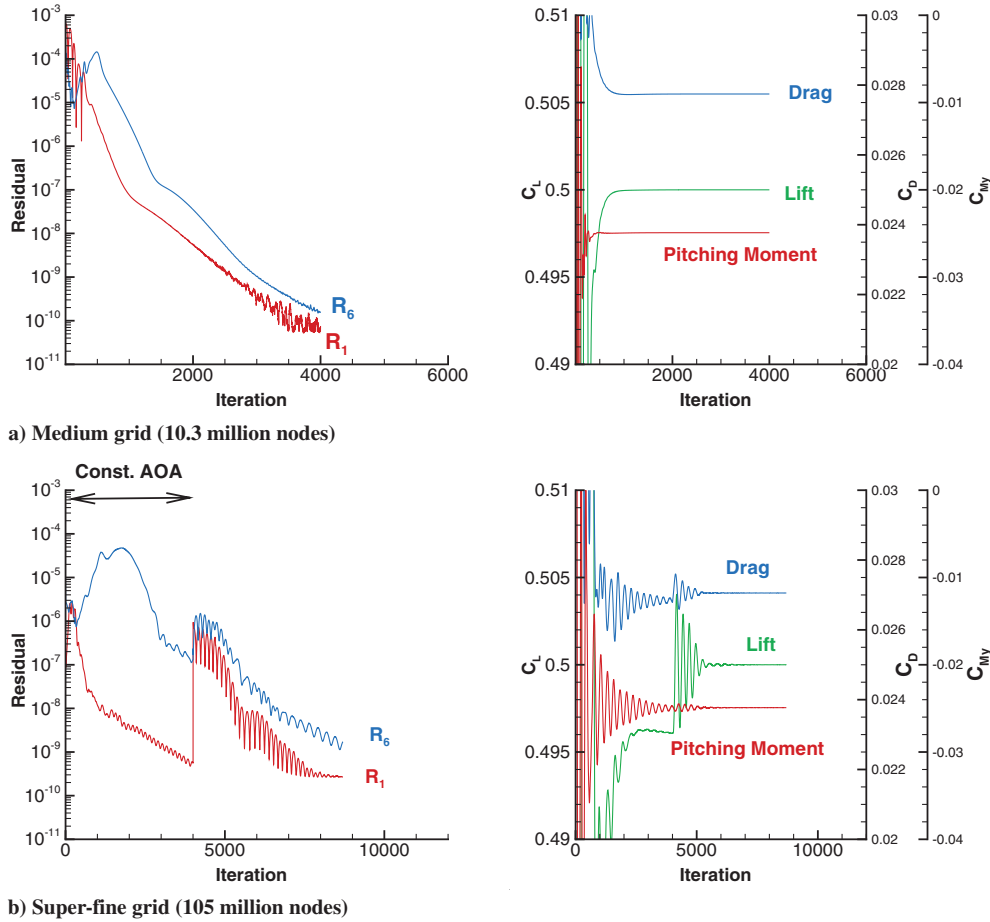


Fig. 4 Nonlinear solution residual, force, and moment convergence history for the CRM wing-body-tail.

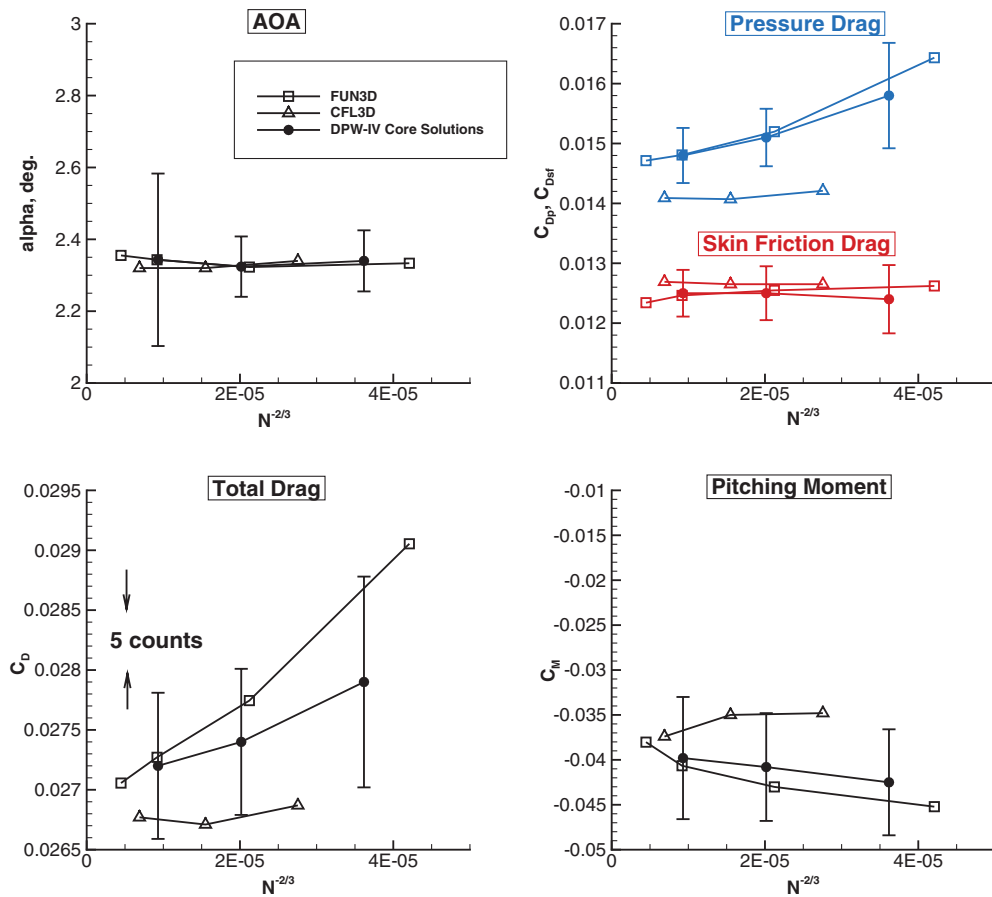


Fig. 5 Grid convergence of CRM total forces and moment at  $M_\infty = 0.85$ ,  $Re_c = 5 \times 10^6$ .

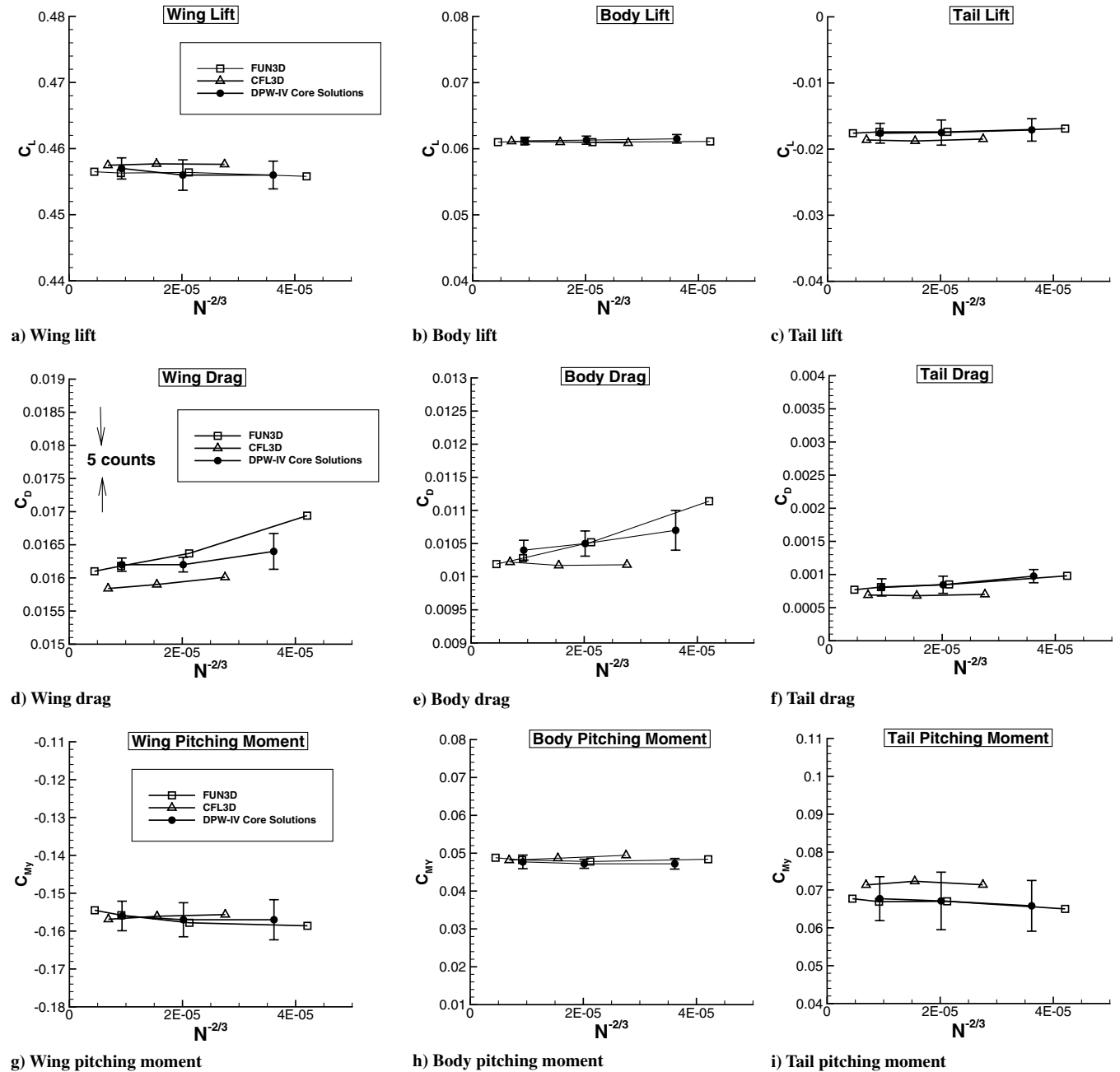


Fig. 6 Grid convergence of CRM component forces and moment at  $M_\infty = 0.85$ ,  $Re_c = 5 \times 10^6$ .

between FUN3D and CFL3D is good. The comparison in total drag between the CFL3D results on finest grid (55 million cells) and the FUN3D results on the fine and super-fine grids is within five drag counts, with most of the variation coming from the pressure component. Similarly, the comparison in pitching moment is quite good at the finest grid levels.

The component forces and moments for the wing, body, and tail are shown in Fig. 6. The CFL3D results [26] and statistical results [16] are also included for comparison. (Note that only 10 of the core solutions provided component forces and moments, and so the statistics are based only on these 10 solutions.) The range of the vertical scales is the same for each component of lift, drag, and pitching moment, which allows for a comparison of variation between the component force and moment contributions. (The data ranges for drag and pitching moment in Fig. 6 are also the same as those shown in Fig. 5.) The FUN3D results in Fig. 6 all lie within one standard deviation of the core solution medians. Figures 6a–6c show that the lift contributions from each of the components is relatively constant with grid refinement. The drag on each of the components

consistently decreases with grid refinement, as shown in Figs. 6d–6f. However, the tail variation is much less than the wing and body variation, which are similar in magnitude. Figures 6g–6i show that the pitching moment contributions from the body and tail are relatively constant with grid refinement, with most of the variation coming from the wing. In comparing the FUN3D results to the CFL3D results, the structured grid solutions consistently have more of a download on the tail, which explains the prediction of a more nose-down tail pitching moment from CFL3D. Figures 6d–6f illustrate that the body and tail drag predictions are very close on the fine grids, with most of the difference in total drag between the FUN3D and CFL3D results coming from the wing component.

Figures 7, 8 show the grid convergence of the wing and tail chordwise pressure coefficient  $C_p$  distributions, respectively. The computational results are shown at selected stations across the wing and tail span that correspond to requested workshop and experimental data locations. (Note that the inset upper-surface pressure line contours are from the fine grid solution.) Figure 7 shows that, on the inboard half of the wing, the differences between the



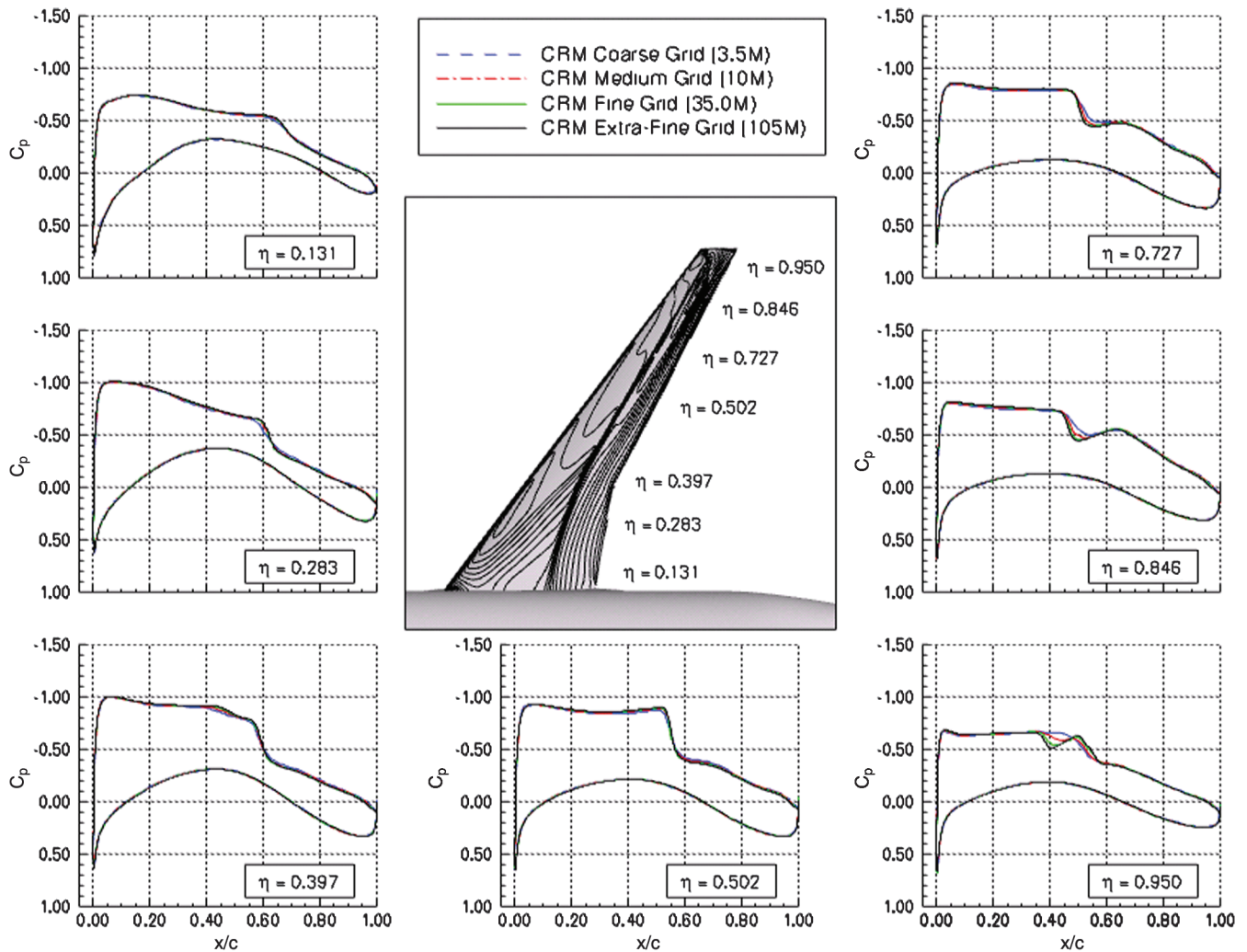


Fig. 7 Grid convergence of CRM wing chordwise pressure distributions at  $M_\infty = 0.85$ ,  $Re_c = 5 \times 10^6$  (surface pressure contours from fine grid solution).

surface pressures on all the grid densities is very small. On the outboard wing, there are more differences in shock strength across the grid range, especially at the tip where the “double shock” structure does not show up at the coarsest grid density. However, the pressure distributions on the fine and super fine grids are very close. Figure 8 shows that the variation in surface pressure with grid refinement is very small across the tail, with only small differences in the leading-edge pressure peak. The wing and tail surface pressures from the FUN3D medium and fine grid solutions are compared to the CFL3D medium grid solutions in Fig. 9. (Note that the fine and medium grid CFL3D pressures distributions are very similar to within plotting accuracy, and so only the medium grid results are shown.) The wing pressures at the midspan location compare very well between the two codes. At the wing-tip location, the overall pressure distribution compares well, except near the double-shock feature, where FUN3D’s two shocks are positioned slightly closer together. The tail pressures at the midspan and tip locations also compare very well between the two codes, with only a slight decrease in nose pressure on the lower surface of the tail for the CFL3D results. This difference could explain the increased tail load predicted with CFL3D.

The CRM fine grid skin friction coefficient and surface-restricted streamlines shown in Fig. 10 illustrate the flow patterns on the wing and tail upper surface. The flow patterns on the fine grid are indicative of those seen on the other grid densities. As was seen in DPW-II and DPW-III, there is an area of flow separation at the trailing edge of the wing-root juncture. There is also a pattern of small trailing-edge separation on the outboard portion of the wing. The grid convergence

of the CRM wing chordwise skin friction distribution at the  $\eta = 0.603$  span station shown in Fig. 11 illustrates that there is a small increase in trailing-edge separation with grid refinement. The effect of grid refinement on the trailing-edge wing-root juncture flow is shown in Fig. 12. In this figure, a close-up of the surface-restricted streamlines on the wing upper surface is shown from a perspective just downstream and outboard of the trailing edge. The comparison of streamline patterns shows an increase in the size of the separated region with grid refinement between coarse, medium, and fine grids, but then very little change between fine and super-fine. No trailing-edge or side-of-body separation was noted on the tail at any grid density. Not all codes in the workshop predicted the same flow patterns on the CRM [1]. Although some codes in the workshop predicted similar patterns of flow separation on the CRM, other codes predicted no wing-root juncture separation and/or no wing trailing-edge separation. Also, some codes predicted a separation pattern on the fuselage just downstream of the tail trailing edge. Although not shown, CFL3D predicted a slightly smaller side-of-body separation region than FUN3D at the medium grid resolution, but the bubble decreased in size as the grid was refined. This may be due to the use of the thin-layer approximation in the CFL3D results. Use of the thin-layer approximation has been shown to reduce the size of the side-of-body separation in DPW-III computations [27].

Figures 13, 14 show the computational results of the downwash study. Figure 13 illustrates the effects of the tail incidence on the CRM total lift, idealized drag, and pitching moment coefficients, where idealized drag is defined as  $C_D - C_L^2/(\pi AR)$ . The CFL3D

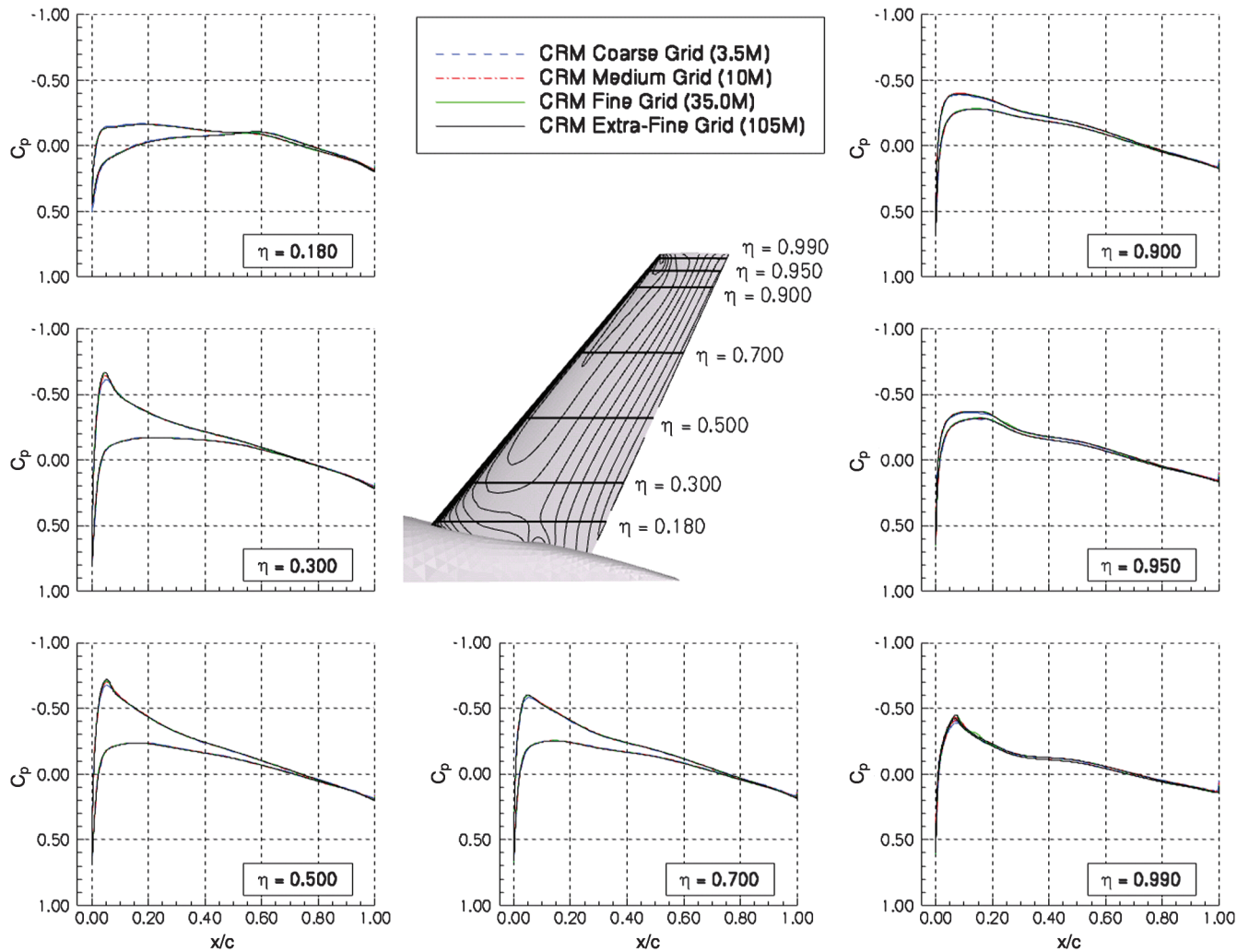


Fig. 8 Grid convergence of CRM tail chordwise pressure distributions at  $M_\infty = 0.85$ ,  $Re_c = 5 \times 10^6$  (surface pressure contours from fine grid solution).

results from [15] are also included in Fig. 13 for comparison. The comparison of lift prediction between the two codes is quite good across the angle of attack and tail incidence range. Similarly, the comparison of pitching moment is also quite good, except at the highest angle of attack. The idealized drag prediction from CFL3D is consistently lower than the FUN3D results across the angle of attack and tail incidence range, except at 4 deg angle of attack, where they are very close. It is interesting to note that, even when the codes do not predict the same absolute values of forces and moments, the deltas due to tail incidence appear to be at the same levels. The trimmed polar forces and moments interpolated from the FUN3D results are shown in Fig. 14 along with the tail-off polar data. The delta drag due to trimming the tail at the design lift coefficient  $C_L = 0.500$  is 27 counts. The range of delta drag due to trimming from the workshop presentations was 27–40 counts [1].

For the case 3 Reynolds-number study, as the Reynolds number was increased to  $Re_c = 20 \times 10^6$ , the angle of attack decreased from 2.32 to 2.14 deg, and the total CRM drag dropped by 33 counts. The drag due to pressure dropped by 21 counts, and the drag due to skin friction dropped by 12 counts. The wing-root juncture separation decreased by about half the size. The range of delta drag due to increased Reynolds number from the workshop presentations was 30–35 counts [1].

## VI. Conclusions

FUN3D Navier–Stokes solutions were successfully computed for the DPW-IV grid-convergence study, downwash study, and

Reynolds-number study on a set of node-based mixed-element grids. All of the baseline tetrahedral grids were generated with the VGRID (developmental) advancing-layer and advancing-front grid-generation software package. Although the grids generated with VGRID were fully tetrahedral, a preprocessing step was used to combine the tetrahedral cells in the boundary-layer portion of the grid into prisms. For the grid-convergence study, a set of four globally refined grids were generated following the gridding guidelines. Similarly, for the downwash study, a set of three consistently sized grids with varying tail incidences were generated. For the tail-off configuration, the tail solid surfaces were removed, and the volume grid was regenerated with the same spacing requirements in the location of the tail as were used in the tail-on configuration. For the high-Reynolds-number grid, the surface grid distribution from the downwash study medium grid was used with a smaller minimum wall spacing. With maximum grid sizes exceeding 100 million nodes, the grid-convergence study was particularly challenging for the node-based unstructured grid generators and flow solvers. At the time of the workshop, the super-fine grid with 105 million nodes and 600 million tetrahedral elements was the largest grid known to have been generated using VGRID. Some improvements to the FUN3D solver/grid processing efficiency and parallelization were shown, which allowed for practical preprocessing and solution times on the largest unstructured-grid size requested for the workshop.

The FUN3D workshop results were computed using the full Navier–Stokes equations with the flux-difference-splitting scheme of Roe, the Venkatakrishnan flux limiter, and the loosely coupled SA turbulence model. Good residual, force, and moment convergence



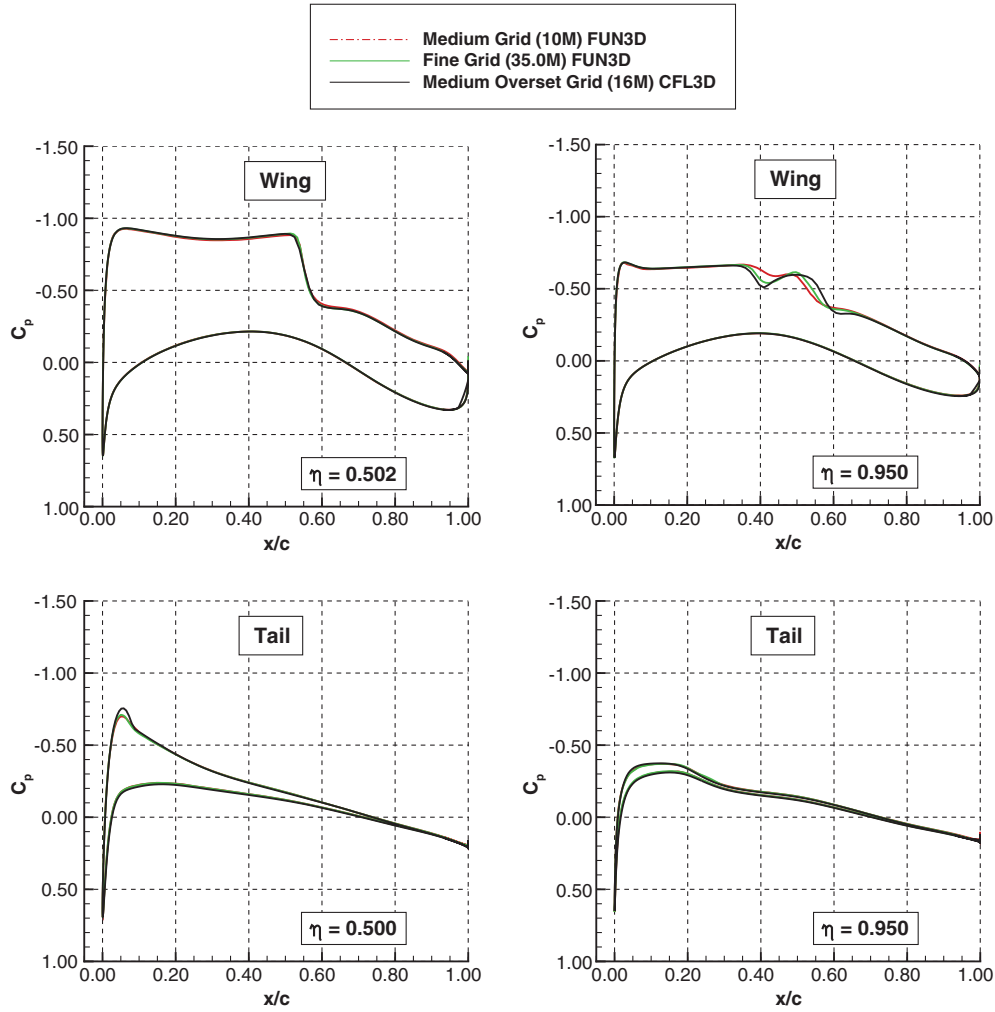


Fig. 9 Comparison of FUN3D and CFL3D CRM wing/tail chordwise pressure distributions at  $M_\infty = 0.85$ ,  $Re_c = 5 \times 10^6$ .

was achieved for the all the workshop computations, even on the super-fine grid size. Overall, the FUN3D results compared well with the structured-grid code CFL3D on the finer grid levels. For the constant-lift grid-convergence case, the convergence of total drag was approximately second-order on the finest three grids. The variation in total drag on the finest three grids was about six counts, and the variation on the finest two grids was two counts. At the finest

grid levels, only small variations in wing and tail pressure distributions were seen with grid refinement. Similarly, a small wing/side-of-body separation also showed little variation at the finest grid levels. For the grid-convergence case, the FUN3D total and component forces/moments were within one standard deviation of the workshop core solution medians and were very close to the median values, especially at the finest grid levels. The FUN3D

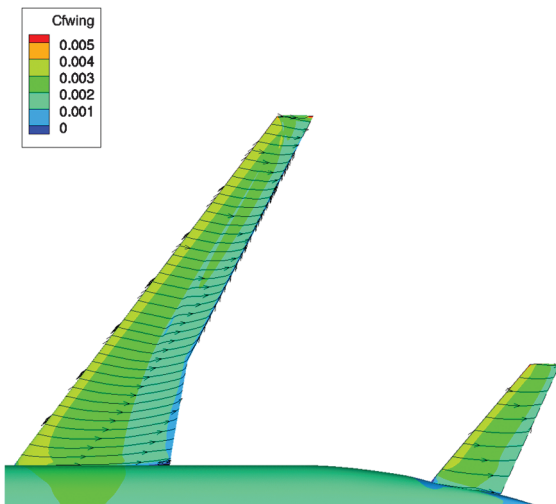


Fig. 10 CRM fine grid (35 million nodes) skin friction coefficient and surface-restricted streamlines at  $M_\infty = 0.85$ ,  $Re_c = 5 \times 10^6$ .

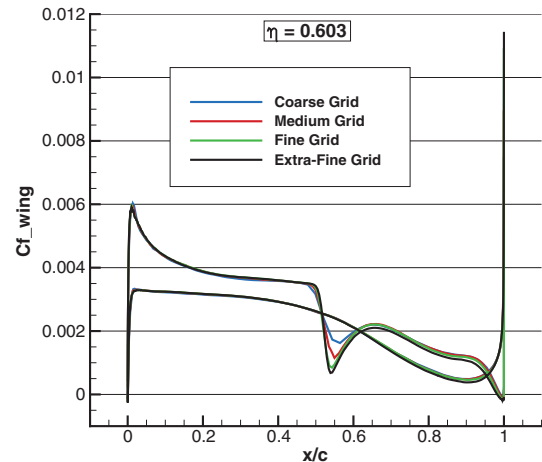


Fig. 11 Grid convergence of CRM wing chordwise skin friction distribution at  $M_\infty = 0.85$ ,  $Re_c = 5 \times 10^6$ .

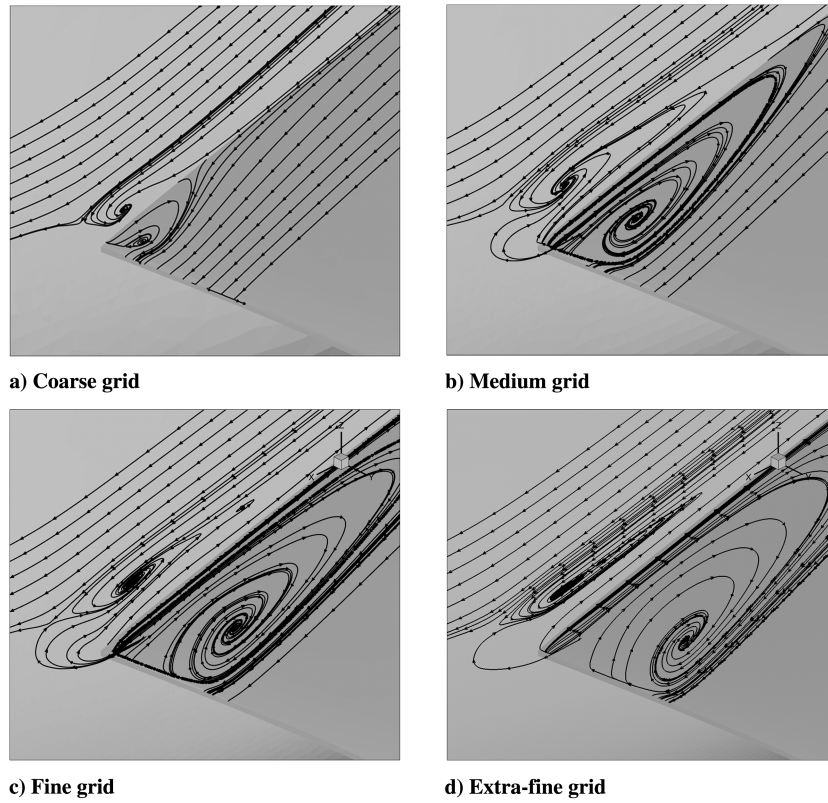


Fig. 12 Effect of grid density on the CRM ( $C_L = 0.5$ ) trailing-edge wing-root junction separation.

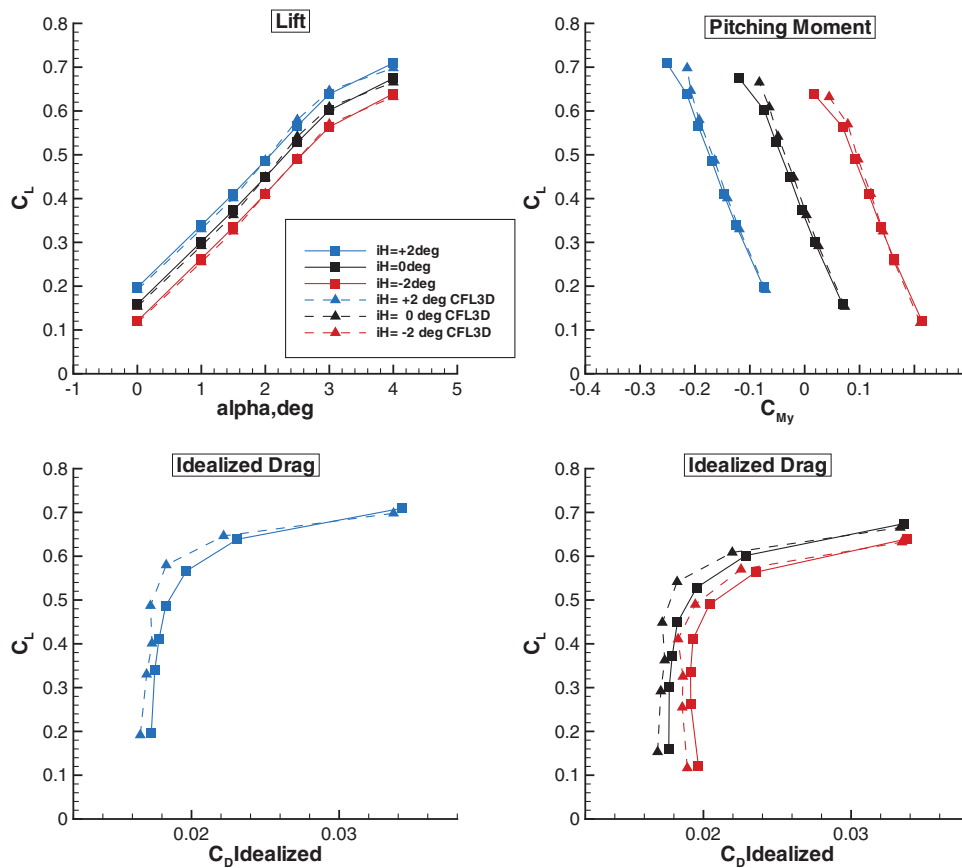


Fig. 13 Effect of tail incidence on CRM forces and moments at  $M_\infty = 0.85$ ,  $Re_c = 5 \times 10^6$ .

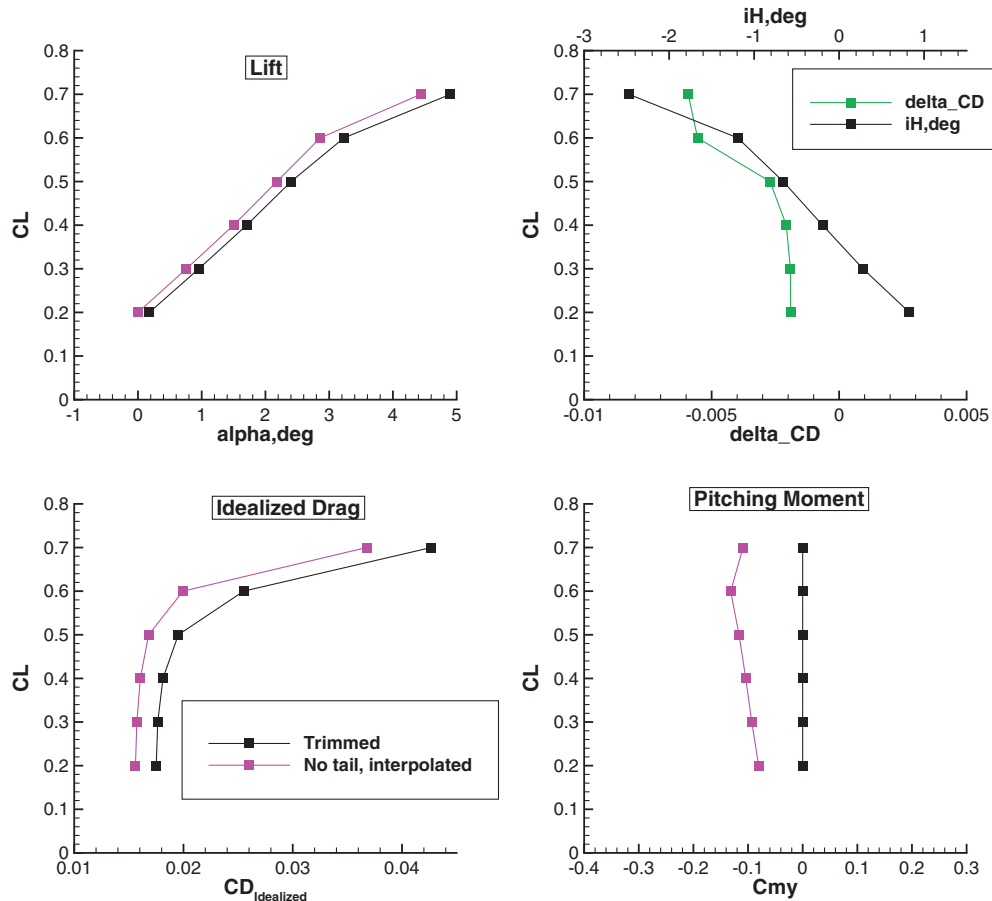


Fig. 14 Comparison of the CRM tail-off and trimmed tail-on forces and moments at  $M_\infty = 0.85$ ,  $Re_c = 5 \times 10^6$ .

downwash study and Reynolds-number study results compared well with the range of results shown in the DPW-IV workshop presentations.

### Acknowledgment

The authors would like to thank Mark Chaffin of the Cessna Aircraft Company for providing the Gridtool restart files for use in the grid-generation process.

### References

- [1] "4th AIAA Drag Prediction Workshop, San Antonio, TX," AIAA, Reston, VA, Dec. 2009, <http://aaac.larc.nasa.gov/tsab/cfdlarc/aiaa-dpw> [retrieved 5 July 2013].
- [2] Levy, D. W., Zickuhr, T., Vassberg, J., Agrawal, S., Wahls, R. A., Pirzadeh, S., and Hemsch, M. J., "Data Summary from the First AIAA Computational Fluid Dynamics Drag Prediction Workshop," *Journal of Aircraft*, Vol. 40, No. 5, 2003, pp. 875–882. doi:10.2514/1.6877; also 40th AIAA Aerospace Sciences Meeting & Exhibit, AIAA Paper 2002-0841, Jan. 2002.
- [3] Laflin, K., Klausmeyer, S., Zickuhr, T., Vassberg, J., Wahls, R., Morrison, J., Brodersen, O., Rakowitz, M., Tinoco, E., and Godard, J.-L., "Data Summary from Second AIAA Computational Fluid Dynamics Drag Prediction Workshop," *Journal of Aircraft*, Vol. 42, No. 5, 2005, pp. 1165–1178. doi:10.2514/1.10771; also 42nd AIAA Aerospace Sciences Meeting and Exhibit, AIAA Paper 2004-0555, May 2004.
- [4] Vassberg, J., Tinoco, E., Mani, M., Brodersen, O., Eisfeld, B., Wahls, R., Morrison, J., Zickuhr, T., Laflin, K., and Mavriplis, D., "Abridged Summary of the Third AIAA Computational Fluid Dynamics Drag Prediction Workshop," *Journal of Aircraft*, Vol. 45, No. 3, March 2008, pp. 781–798; also 45th AIAA Aerospace Sciences Meeting and Exhibit, AIAA Paper 2007-0260, Jan. 2007.
- [5] Vassberg, J. C., DeHaan, M. A., Rivers, S. M., and Wahls, R. A., "Development of a Common Research Model for Applied CFD Validation Studies," 26th AIAA Applied Aerodynamics Conference, AIAA Paper 2008-6919, Aug. 2008.
- [6] Rivers, M. B., and Dittberner, A., "Experimental Investigations of the NASA Common Research Model (Invited)," 28th AIAA Applied Aerodynamics Conference, AIAA Paper 2010-4218, June 2010.
- [7] Rivers, M. B., and Dittberner, A., "Experimental Investigations of the NASA Common Research Model in the NASA Langley National Transonic Facility and NASA Ames 11-Ft Transonic Wind Tunnel (Invited)," 49th AIAA Aerospace Sciences Meeting, AIAA Paper 2011-1126, Jan. 2011.
- [8] Rivers, M. B., and Hunter, C. A., "Support System Effects on the NASA Common Research Model," 50th AIAA Aerospace Sciences Meeting, AIAA Paper 2012-0707, Jan. 2012.
- [9] Rivers, M. B., Hunter, C. A., and Campbell, R. L., "Further Investigation of the Support System Effects and Wing Twist on the NASA Common Research Model," 30th AIAA Applied Aerodynamics Conference, AIAA Paper 2012-3209, June 2012.
- [10] Eliasson, P., and Peng, S., "Influence of Turbulence Modelling and Grid Resolution in Computations of the DPW-4 CRM Configuration," 48th AIAA Aerospace Sciences Meeting, AIAA Paper 2010-1416, Jan. 2010.
- [11] Hashimoto, A., Murakami, K., Aoyama, T., Yamamoto, K., Murayama, M., and Lahur, P. R., "Drag Prediction on NASA CRM Using Automatic Hexahedra Grid Generation," 48th AIAA Aerospace Sciences Meeting, AIAA Paper 2010-1417, Jan. 2010.
- [12] Anderson, W. K., and Bonhaus, D. L., "An Implicit Upwind Algorithm for Computing Turbulent Flows on Unstructured Grids," *Computers and Fluids*, Vol. 23, No. 1, 1994, pp. 1–22. doi:10.1016/0045-7930(94)90023-X
- [13] Anderson, W. K., Rausch, R. D., and Bonhaus, D. L., "Implicit/Multigrid Algorithms for Incompressible Turbulent Flows on Unstructured Grids," *Journal of Computational Physics*, Vol. 128, No. 2, 1996, pp. 391–408. doi:10.1006/jcph.1996.0219
- [14] Nielsen, E. J., "Aerodynamic Design Sensitivities on an Unstructured Mesh Using the Navier–Stokes Equations and a Discrete Adjoint Formulation," Ph.D. Thesis, Virginia Polytechnic Inst. and State Univ., Blacksburg, VA, 1998.
- [15] Sclafani, A. J., Vassberg, J. C., Rumsey, C. L., and DeHaan, M. A., "Drag Prediction for the NASA CRM Wing/Body/Tail Using CFL3D

- and OVERFLOW on an Overset Mesh,” *28th AIAA Applied Aerodynamics Conference*, AIAA Paper 2010-4219, June 2010.
- [16] Morrison, J., “Statistical Analysis of CFD Solutions from the Fourth AIAA Drag Prediction Workshop,” *28th AIAA Applied Aerodynamics Conference*, AIAA Paper 2010-4673, June 2010.
- [17] Pirzadeh, S. Z., “Advanced Unstructured Grid Generation for Complex Aerodynamic Applications,” *AIAA Journal*, Vol. 48, No. 5, 2010, pp. 904–915. doi:10.2514/1.41355; also *26th AIAA Applied Aerodynamics Conference*, AIAA Paper 2008-7178, Aug. 2008.
- [18] Pirzadeh, S. Z., and Frink, N. T., “Assessment of the Unstructured Grid Software TetrUSS for Drag Prediction of the DLR-F4 Configuration,” *40th AIAA Aerospace Sciences Meeting & Exhibit*, AIAA Paper 2002-0839, Jan. 2002.
- [19] Roe, P. L., “Approximate Riemann Solvers, Parameter Vectors, and Difference Schemes,” *Journal of Computational Physics*, Vol. 43, No. 2, 1981, pp. 357–372.  
doi:10.1016/0021-9991(81)90128-5
- [20] Venkatakrishnan, V., “Convergence to Steady State Solutions of the Euler Equations on Unstructured Grids with Limiters,” *Journal of Computational Physics*, Vol. 118, No. 1, 1995, pp. 120–130.  
doi:10.1006/jcph.1995.1084
- [21] Anderson, W. K., and Bonhaus, D. L., “An Implicit Upwind Algorithm for Computing Turbulent Flow on Unstructured Grids,” *Computers and Fluids*, Vol. 23, No. 1, 1994, pp. 1–21.  
doi:10.1016/0045-7930(94)90023-X
- [22] Diskin, B., Thomas, J. L., Nielsen, E. J., and White, J. A., “Comparison of Node-Centered and Cell-Centered Unstructured Finite-Volume Discretizations Part 1: Viscous Fluxes,” *47th AIAA Aerospace Sciences Meeting*, AIAA Paper 2009-0597, Jan. 2009.
- [23] Nielsen, E. J., Lu, J., Park, M. A., and Darmofal, D. L., “An Implicit, Exact Dual Adjoint Solution Method for Turbulent Flows on Unstructured Grids,” *Computers and Fluids*, Vol. 33, No. 9, 2004, pp. 1131–1155. doi:10.1016/j.compfluid.2003.09.005; also *41st Aerospace Sciences Meeting and Exhibit*, AIAA Paper 2003-0272, Jan. 2003.
- [24] Spalart, P. R., and Allmaras, S. R., “A One-Equation Turbulence Model for Aerodynamic Flows,” *La Recherche Aerospaciale*, Vol. 1, No. 1, 1994, pp. 5–21; also *30th Aerospace Sciences Meeting and Exhibit*, AIAA Paper 1992-0429, Jan. 1992.
- [25] Menter, F. R., “Two-Equation Eddy-Viscosity Turbulence Models for Engineering Applications,” *AIAA Journal*, Vol. 32, No. 8, 1994, pp. 1598–1605.  
doi:10.2514/3.12149
- [26] Krist, S. L., Biedron, R. T., and Rumsey, C. L., “CFL3D User’s Manual,” Ver. 5.0, NASA TM-1998-208444, June 1998.
- [27] Sclafani, A. J., Vassberg, J. C., Harrison, N. A., DeHaan, M. A., Rumsey, C. L., Rivers, S. M., and Morrison, J. H., “CFL3D/OVERFLOW Results for DLR-F6 Wing/Body and Drag Prediction Workshop Wing,” *Journal of Aircraft*, Vol. 45, No. 3, 2008, pp. 762–780.  
doi:10.2514/1.30571